



# Rapid Deformation Calculation for Large Reflector Antennas: A Surrogate Model Method

Zi-Han Zhang<sup>1</sup> , Qian Ye<sup>2,\*</sup>, Li Fu<sup>2</sup>, Jin-Qing Wang<sup>2</sup>, Meng Guo-Xiang<sup>1</sup>, and Zhi-Qiang Shen<sup>2</sup>

<sup>1</sup> School of Mechanical Engineering, Shanghai Jiao Tong University, Shanghai 200240, China; [zhangyueban@sjtu.edu.cn](mailto:zhangyueban@sjtu.edu.cn), [guoxiangm@yahoo.co.jp](mailto:guoxiangm@yahoo.co.jp)  
<sup>2</sup> Shanghai Astronomical Observatory, Chinese Academy of Sciences, Shanghai 200030, China; [yeqian@shao.ac.cn](mailto:yeqian@shao.ac.cn), [fuli@shao.ac.cn](mailto:fuli@shao.ac.cn), [jqwang@shao.ac.cn](mailto:jqwang@shao.ac.cn), [zshen@shao.ac.cn](mailto:zshen@shao.ac.cn)

Received 2022 August 17; revised 2022 October 9; accepted 2022 October 21; published 2022 December 9

## Abstract

The surface accuracy of the large-aperture reflector antenna has a significant influence on the observation efficiency. Recent researchers have focused on using the finite element (FE) simulation to study the effect of gravity and heat on the deformation distribution of the main reflector. However, the temperature distribution of the antenna is challenging to obtain, and it takes a long time for the FE simulation to carry out FE modeling and post-processing. To address these limitations, this study presents a surrogate model based on Extreme Gradient Boosting (XGBoost) and deep Convolutional Neural Network (CNN) to get the deformation distribution of the main reflector quickly. In the design of the surrogate model, using the XGBoost algorithm and sparse sampling to solve the difficulty of obtaining the entire temperature distribution is first proposed, and then a deep CNN is developed for estimating deformation. Based on the effect of dynamic loads on the antenna structure, a diverse data set is generated to train and test the surrogate model. The results show that the surrogate model reduces the calculating time dramatically and can obtain the indistinguishable deformation compared to the FE simulation. This technique provides a valuable tool for temperature and deformation calculation of large-aperture antennas.

*Key words:* telescopes – methods: analytical – methods: numerical – methods: data analysis

## 1. Introduction

Large-aperture reflector antennas are widely used in communication, radar, and radio astronomy. The surface error and its distribution of an antenna, which are caused by dynamic loads (e.g., gravity, heat, and wind, Sun et al. 2021), directly determine the work efficiency of the antenna (Lian et al. 2015). To eliminate the surface error, the active surface design is applied to the main reflector of the fully movable antennas, such as America GBT 100×110 m, Italy SRT 64 m, and China TM 65 m antenna (Wang et al. 2018). Therefore, high-accuracy and real-time deformation calculation are of great significance to improve the efficiency of the antenna.

The studies of using finite element (FE) simulation to analyze the deformation of the main reflector caused by gravity and heat have been mature. In dynamic loads, gravity is the dominant factor causing the deformation of the main reflector. The gravity-induced deformation distribution varies with elevation angle and can be simulated by the antenna FE model (Wang et al. 2014; Hu et al. 2017; Bergstrand et al. 2019; Lian et al. 2021). The temperature distribution of the antenna is always time-varying, which will cause irregular deformation. Therefore, studying the temperature distribution and thermal-structure coupled analysis of the main reflector of the large-

aperture antenna is very significant. In many literatures, through FE simulations and experimental tests, the temperature distribution and thermal-induced deformation of the main reflector have been studied (Greve et al. 2005; Li et al. 2012; Liu 2016). Most of the above FE analysis applications to calculate the gravity-thermal-induced deformation follow a similar workflow, as shown in the left flow chart in Figure 1: (i) manually establish the FE model of the antenna. (ii) Obtain the approximate temperature distribution of the antenna according to the FE method based on heat exchange theory or arranging a large number of temperature sensors. (iii) Apply thermal and gravity loads; perform the FE simulation by specialized software, and then the least-squares method is used to calculate the best-fitting paraboloid.

However, current FE simulation workflows have such limitations: (i) theoretically, both direct measurement and indirect calculation methods can be used to obtain the temperature distribution of the main reflector. However, direct measurement needs a considerable number of temperature sensors, which will affect the surface accuracy of the antenna, and the indirect calculation method based on thermal environment exchange requires complex FE simulation. Most researchers are still unable to measure the temperature distribution of the main reflector of large-aperture antennas accurately and quickly (Wei et al. 2021), resulting in inability

\* Corresponding author.

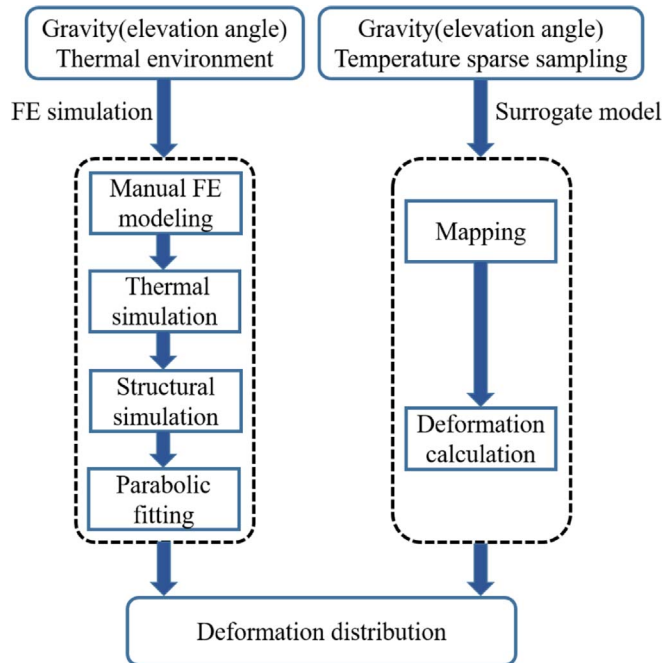


Figure 1. The current FE analysis workflow and the surrogate model.

to calculate thermal deformation accurately. (ii) The time spent on manual FE modeling, thermal-structure coupled analysis and post-processing is incalculable, possibly tens of minutes or hours, which makes the FE simulation results lag behind the deformation distribution changes. With the increasing demand for real-time surface adjustment of large-aperture antennas, the shortcomings of current workflows limit the application of FE analysis to deformation calculations. In addition to the FE simulation, other mature methods (e.g., photogrammetric measurement, Subrahmanyam 2005, out-of-focus holography, Nikolic et al. 2007a, 2007b; Dong et al. 2018b, etc.) have also been used to obtain the deformation of the main reflector surface, but the measurement accuracy depends on the operating environment and equipment.

The emergence of machine learning provides new methods for solving nonlinear problems. In recent years, many researchers have used machine learning models, especially deep learning models, to replace time-consuming and complex works, and these models are referred to as surrogate models. The surrogate models have been proposed in many fields, such as medical diagnosis (Liang et al. 2017,2018), stamping quality assessment (Attar et al. 2021; Lee et al. 2021), structural optimization (Mai et al. 2021), and topology optimization (Sato & Igarashi 2022). Moreover, for variables whose entire spatial distributions are difficult to obtain, sparse sampling with the machine learning method has been proved to be effective for spatial distribution prediction (Qu et al. 2020; Zheng et al. 2022). The application of machine learning in the study of the deformation of the antenna’s main reflector is not yet mature. In

Wang et al. 2022, an artificial neural network was proposed as an approximator to fit the deformation-amplitude equation (DAE), but the basis of the mathematical model still requires a lot of prior knowledge.

To solve the limitations, we take TM 65 m antenna as the research object and propose a surrogate model containing two modules, as shown in the right flow chart in Figure 1. The mapping module contains gravity mapping based on linear mapping and temperature mapping based on the Extreme Gradient Boosting (XGBoost) algorithm. The deep Convolutional Neural Network (CNN) is used to calculate the deformation distribution of the main reflector. The surrogate model can estimate the deformation in real time and only need sparse information containing elevation angle and temperature data obtained by sparse sampling.

## 2. Overview of the Surrogate Model Method

The overall workflow of the surrogate model is shown in Figure 2. First, dynamic loads containing gravity and temperature from design choices are mapped to a suitable form. The elevation angle is converted to a set of values referred to as attitude code by a linear mapping without parameters to be trained. For the mapping of temperature distribution, sparse sampling is first performed by arranging a small number of temperature feature points that represent the temperature sensors on the main reflector, and then the temperature data of feature points are mapped to the entire temperature distribution of the main reflector by a nonlinear mapping, which needs to be achieved by the trained XGBoost algorithm. Second, the attitude code and temperature distribution are taken as the input of the deep CNN, and the deformation distribution is taken as the output target of the deep CNN. It should be noted that the XGBoost algorithm and the deep CNN model are trained and validated separately through the FE simulation data set, and then two modules are combined to constitute a surrogate model. Once the surrogate model is trained and tested, it can be used to monitor the deformation of the antenna’s main reflector in real time. The data required by this method are only the elevation angle value and the temperature of the feature points which can be obtained by arranging a small number of contact temperature sensors.

Based on the fact that there is still no absolutely accurate method for calculating the temperature and deformation of the large-aperture antenna’s main reflector. Using the FE analysis verified on many antennas as the standard, we compare the surrogate model method with the FE simulation to demonstrate its advantages. The details of each step of the surrogate model are described in the following sections.

## 3. Finite-Element Simulation Dataset

To train the XGBoost model and the deep CNN model, the FE simulation of the antenna was used to generate samples for

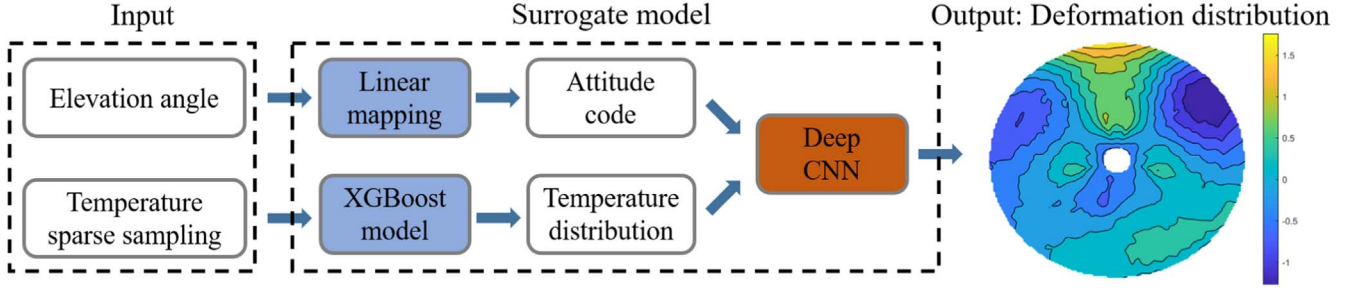


**Figure 2.** The overall workflow of the surrogate model.

training, validating, and testing the surrogate model. Traditionally, the machine learning model requires a diverse data set including a numerous amount of samples to train the parameters of models (Sha & Edwards 2007). We employed the batch application in FE software to generate samples. The details of thermal-structural FE simulation and the process of deformation calculation are provided in this section.

### 3.1. FE Simulation of the Antenna

As shown in Figure 3, the FE model of the TM 65 m antenna was established with FE software. The antenna structure includes the main reflector, the minor reflector, the frame carrier, the minor reflector support, the central tube, the pitch mechanism, the azimuth bear, the drive unit, and the actuator. According to the actual situation, some parts were replaced by mass-node elements in the FE model. The main reflector of the TM 65 m antenna consists of 1008 panels, which are divided into 14 rings. A total of 1104 actuators are used to support and adjust the reflector surface to ensure the work efficiency of the antenna. Therefore, the FE model of the main reflector contains 1008 elements and 1104 nodes, as shown in Figure 4.

A qualified data set should provide diverse samples to ensure the model's robustness. We spent a long time generating FE models with different elevation angles, ranging from  $5^\circ$  to  $90^\circ$ . The change in the elevation angle means that the gravity distribution of the entire antenna has changed, which induces the dominant deformation of the antenna. These FE models have been verified to have a high similarity with the actual antenna, and already applied to the deformation compensation of the TM 65 m antenna's main reflector (Fu et al. 2017).

Compared with the elevation angle, the natural environment causes the antenna temperature and deformation to be more random and variable. A program for randomly changing the thermal environment of the antenna FE model was established, and the diverse temperature distributions of the entire antenna were obtained through FE simulation, as shown in Figure 5.

The simulated thermal and gravitational loads were applied to the antenna models with different elevation angles, and then the structural FE simulations were computed by the FE solver. However, for a fully movable antenna, the displacement of the

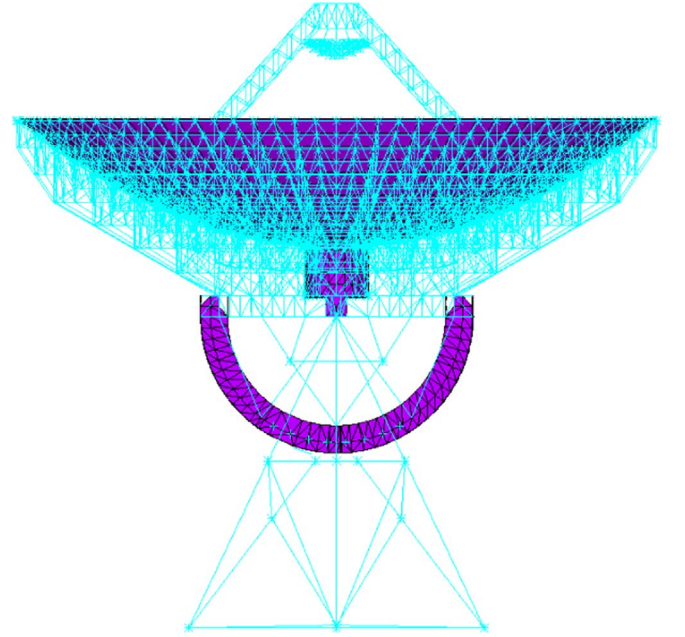


**Figure 3.** The FE model of the antenna at an elevation angle of  $90^\circ$ .

main reflector obtained by the FE simulation does not represent the deformation of the main reflector, which should be obtained by calculating the normal error between the deformed surface and the best-fitting paraboloid. The best-fitting paraboloid was fitted according to the displacement of the main reflector, as shown in Figure 6. There are six parameters used to determine the geometry position of the best-fitting paraboloid:  $\Delta x$ ,  $\Delta y$ ,  $\Delta z$ ,  $\varphi_x$ ,  $\varphi_y$ ,  $\Delta f$ .  $\Delta x$ ,  $\Delta y$ , and  $\Delta z$  represent the X, Y, and Z components of the displacement of the paraboloid vertex, respectively;  $\varphi_x$  and  $\varphi_y$  represent the rotation angle of the paraboloid around the X-axis and Y-axis; since the paraboloid is symmetric about the Z-axis,  $\varphi_z$  was omitted;  $\Delta f$  represents the change in focal length. For a vector represented as  $(x, y, z)$  in the old coordinate system, it is described as  $(x', y', z')$  in the new coordinate system, and the relationship between coordinates in the new and the old coordinate systems is shown in Equation (1), the rotation angles  $\varphi_x$  and  $\varphi_y$  are very

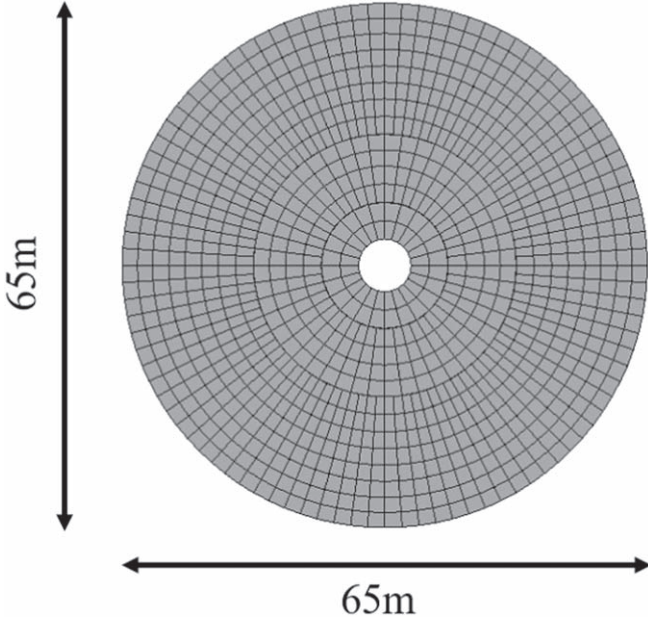


Figure 4. The main reflector of the TM 65 m antenna.

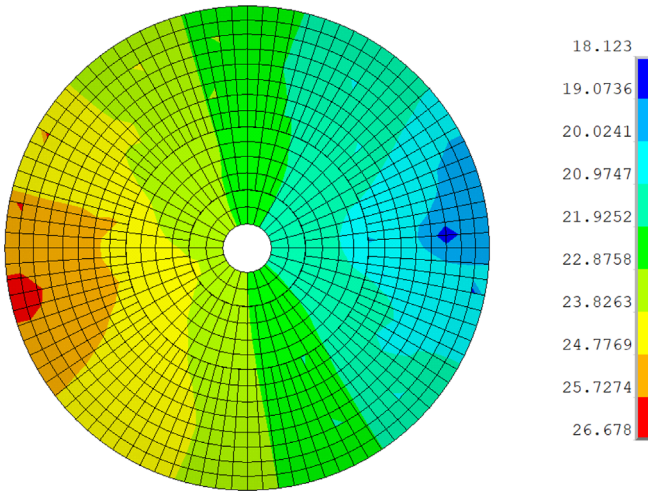


Figure 5. Temperature distribution of the main reflector.

small, so  $\cos \varphi_x \approx 1$ ,  $\cos \varphi_y \approx 1$ ,  $\sin \varphi_x \approx \varphi_x$ ,  $\sin \varphi_y \approx \varphi_y$ .

$$\begin{aligned} x' &= x - \Delta x - z\varphi_y \\ y' &= y - \Delta y + z\varphi_x \\ z' &= z - \Delta z + x\varphi_y - y\varphi_x \end{aligned} \quad (1)$$

The design paraboloid and the best-fitting paraboloid can be defined as Equations (2) and (3), respectively.

$$z = \frac{1}{4f}(x^2 + y^2) \quad (2)$$

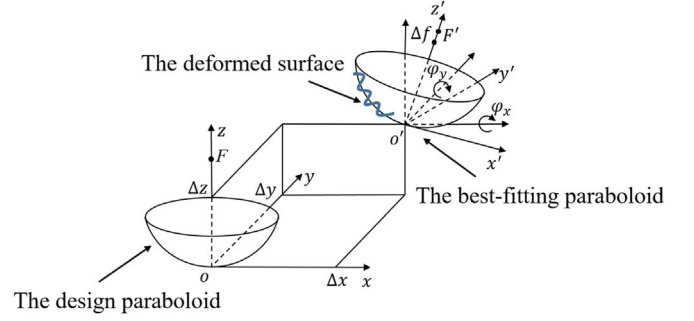


Figure 6. The relationship between the three surfaces (the design paraboloid, the deformed surface, and the best-fitting paraboloid).

$$z' = \frac{1}{4(f + \Delta f)}(x'^2 + y'^2). \quad (3)$$

The best-fitting paraboloid expressed in the old Cartesian coordinate system can be obtained through Equations (1)–(3) and is shown in Equation (4) (Wu et al. 2021). The higher-order terms of the six parameters were omitted in the calculation process.

$$z = \frac{x^2 + y^2 - 2x(\Delta x + 2f\varphi_y) - 2y(\Delta y - 2f\varphi_x) + 4f\Delta z}{-2y\varphi_x + 2x\varphi_y + 4(f + \Delta f)}. \quad (4)$$

The least-squares method was used to solve the six parameters of the best-fitting paraboloid, and then the surface normal error value between the deformed surface and the best-fitting paraboloid was calculated. The axial error between the deformed surface and the best-fitting paraboloid surface can be defined as Equation (5); and the normal error can be defined as Equation (6) based on the parabolic geometry theory (Fu et al. 2015).

$$\delta_z = z_1 - z_0 \quad (5)$$

$$\delta_n = \frac{\delta_z f}{\sqrt{f(f + z_p)}}, \quad (6)$$

where  $z_0$ ,  $z_1$ , and  $z_p$  represent the Z-coordinates of a node on the best-fitting paraboloid, the deformed surface, and the design paraboloid, respectively.

The goal of the least-squares method is to calculate the parameters of the best-fitting paraboloid to minimize the objective function, as shown in Equation (7). According to the extreme value theorem of calculus, the objective function takes the minimum value when Equation (8) is established (Wu et al. 2021).

$$\Delta_D^2 = \sum_{i=1}^M \delta_{n_i}^2, \quad (7)$$

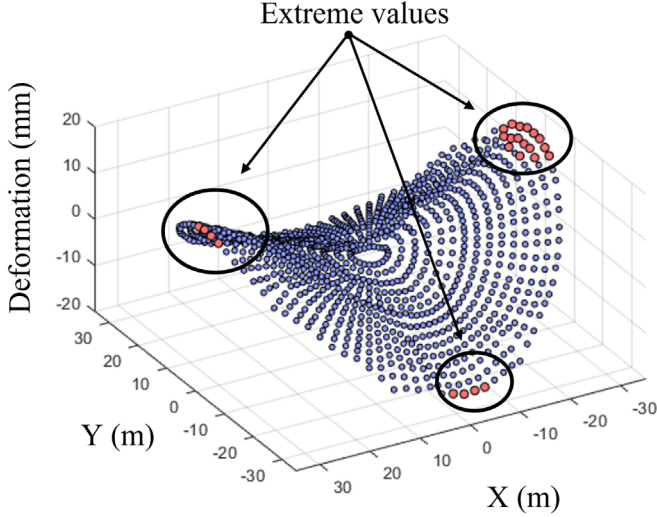


Figure 7. Deformation distribution with numerical outliers.

where  $M$  is the number of nodes on the main reflector.

$$\begin{aligned} \frac{\partial \Delta_D^2}{\partial \Delta x} &= \frac{\partial \Delta_D^2}{\partial \Delta y} = \frac{\partial \Delta_D^2}{\partial \Delta z} \\ &= \frac{\partial \Delta_D^2}{\partial \varphi_x} = \frac{\partial \Delta_D^2}{\partial \varphi_y} = \frac{\partial \Delta_D^2}{\partial \Delta f} = 0. \end{aligned} \quad (8)$$

### 3.2. Data Preparation

Before using the data set to train the surrogate model, the quality of the samples was evaluated to ensure that a high-quality data set was obtained. In the batch generated samples, there may be implausible samples that affect the accuracy of the model. Our method focuses on calculating the deformation caused by dynamic loads rather than the large range deformation caused by mechanical factors, so we defined samples containing deformation data exceeding  $\pm 15$  mm as extreme samples that need to be removed. This range is the adjustable distance of the actuators on the TM 65 m antenna and is much larger than the deformation size caused by the dynamic loads according to previous studies (Qian et al. 2012; Fu et al. 2017; Dong et al. 2018a; Dong & Liu 2021). Figure 7 shows an example of an extreme sample. Overall, a sample generation pipeline was developed to generate 5000 quality assured samples, and each sample contains attitude, temperature, and deformation data represented by a discrete set of nodes.

## 4. XGBoost Model for Temperature Mapping

### 4.1. Sparse Sampling and the Feature Points

In the actual temperature measurement of the large-aperture antenna, it is impossible to arrange a considerable number of

temperature sensors to obtain the entire temperature distribution. The mapping of the temperature of feature points to entire temperature distribution is achieved by appropriate sparse sampling and the XGBoost algorithm. Both the location and number of feature points will affect the estimation accuracy of the temperature distribution. Since the temperature environment of the antenna is complex, it is necessary to arrange the feature points uniformly to eliminate the influence of different location distribution of feature points. Therefore, the location of temperature feature points was selected by the K-means clustering algorithm. As shown in Equation (9), the objective of clustering is to minimize the sum of the distance between each node on the main reflector and the center point of the area to which this node belongs (Hartigan & Wong 1979). The center point of each class was selected as the feature point, which is the location of the temperature sensor. In order to train the XGBoost model, the temperature values of feature points were selected as the input of the XGBoost machine learning model; the temperature distribution of the main reflector surface including 1104 nodes was taken as the output of the XGBoost model.

$$D = \sum_{i=1}^M \|p_i - \mu_{c_i}\|^2, \quad (9)$$

where  $M$  is the total number of nodes,  $p_i$  is the location of node  $i$ ,  $c_i$  is the area to which node  $i$  belongs, and  $\mu_{c_i}$  is the location of center point.

### 4.2. Extreme Gradient Boosting Algorithm

The XGBoost algorithm (Chen & Guestrin 2016) is an ensemble learning method based on the idea of “boosting,” and its fundamental approach is to cultivate a “strong” learner with high accuracy through multiple simple “weak” learners. The goal of the XGBoost algorithm is to obtain accurate predictions while preventing overfitting, which is achieved by adding regularization terms to the loss function (Fan et al. 2018). The XGBoost calculation workflow is shown in Figure 8. The initial training samples are used to train the first learner, and then the residuals between the prediction values and the label values are calculated. The objective of the second learner is to fit residuals, and then the sum of the first learner and second learner will have fewer residuals. The calculation process is repeated until the number of learners reaches the specified value or the entire ensemble result reaches the accuracy condition. The final prediction of the model is obtained by a weighted combination of predictions from each learner. The general function for the prediction of the  $i$ th sample at step  $t$  is presented as follows:

$$\hat{y}_i^t = \hat{y}_i^{t-1} + f_t(x_i), \quad (10)$$

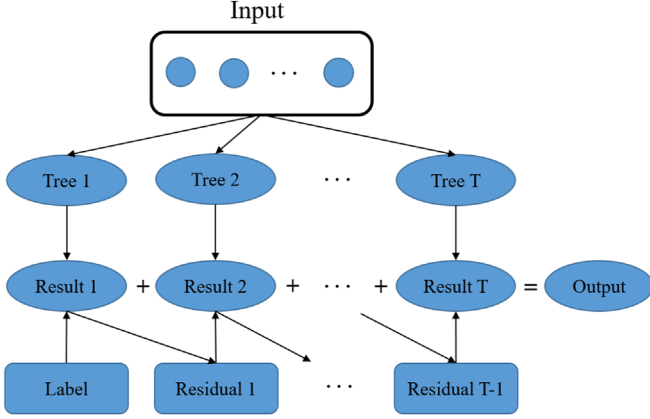


Figure 8. Flowchart of the XGBoost algorithm.

where  $f_t(x_i)$  is the prediction result of the learner at step  $t$ ;  $\hat{y}_i^{t-1}$ , a known constant, is the prediction at step  $t-1$ ; and  $\hat{y}_i^t$  is the prediction at step  $t$ .

To avoid the overfitting problem without affecting the computational speed of the model, the XGBoost model derives the following analytical expression as the objective function at step  $t$ :

$$L^t = \sum_{i=1}^n l(\hat{y}_i^{t-1}, \hat{y}_i^t) + \sum_{i=1}^t \Omega(f_i), \quad (11)$$

where  $l$  is the loss function,  $n$  is the total number of samples, and  $\Omega(f_i)$  is the regularization term to prevent overfitting.

The regularization term is defined by

$$\Omega(f) = \gamma k + \frac{1}{2} \lambda \|\omega\|^2, \quad (12)$$

where  $\gamma$  is the complexity parameter,  $k$  is the number of leaves,  $\gamma k$  represents the complexity of the learner,  $\lambda$  is the regularization parameter, and  $\omega$  is the weight vector of leaf nodes.

Of the 5000 samples, 3000 samples were used for training the model's parameters, 1000 samples were used for verifying the model's performance preliminarily, and 1000 samples were used for testing the generalization of the trained model. The model was trained using the temperature values of feature points as input and the theoretical temperature distribution generated by FE simulation as output. In the test process, the root mean squared error (rms), as shown in Equation (13), and the relative root mean square error (RRMS), as shown in Equation (14), were selected as performance metrics to evaluate the accuracy of the temperature distribution estimated by the XGBoost machine learning model.

$$\text{RMS} = \sqrt{\frac{\sum_{i=1}^M (t_i - \tilde{t}_i)^2}{M}} \quad (13)$$

$$\text{RRMS} = \frac{\text{RMS}}{t_{\max} - t_{\min}}, \quad (14)$$

where  $t_i$  is a theoretical temperature value at node  $i$ ,  $\tilde{t}_i$  is a temperature value estimated from the XGBoost machine learning model,  $t_{\max}$  is the maximum temperature for each sample, and  $t_{\min}$  is the minimum temperature for each sample.

## 5. Deep Learning Model

### 5.1. The Input and Output of the Deep CNN

Gravity and heat, which are the main factors affecting the surface accuracy of the antenna reflector, were considered as the input of the deep CNN model. The gravity and temperature from the design choice were first mapped to suitable forms for training the deep CNN. We took the Z component of the nodes' coordinate values in the global coordinate system as the attitude code to completely replace the gravity information for the following two theoretical reasons: (i) The gravity-induced deformation is caused by changes in elevation angle. (ii) According to the main reflector's rotational motion, each elevation angle corresponds to a unique set of Z-coordinate values. Overall, the attitude code obtained from elevation angle and the temperature distribution generated by the FE simulation were taken as the input of the deep CNN model, and the output of the deep CNN model was the deformation of the main reflector surface.

It should be highlighted that the input and output of the deep CNN model are images with a unified representation. The interpolation method was used to transform the data into matrices with the same size,  $128 \times 128$  pixels, as shown in Figure 9. In order to make the network more directly learn the relationship between input and output, the deep CNN was trained by matrices where each pixel value represents the actual data of temperature, attitude code, or deformation value instead of the color value. Once the data has been processed, the input size of the deep CNN is  $128 \times 128 \times 2$ , and the output size of the deep CNN is  $128 \times 128 \times 1$ . The data was normalized by applying Equation (15) to eliminate the influence of dimension.

$$x_{\text{new}} = \frac{x - x_{\min}}{x_{\max} - x_{\min}}, \quad (15)$$

where  $x$  is the initial value,  $x_{\text{new}}$  is the normalized value,  $x_{\min}$  is the minimum in this kind of data, and  $x_{\max}$  is the maximum in this kind of data.

### 5.2. The Structure of the Deep CNN

In this paper, a deep CNN model was developed from the following aspects: (i) the input of the model is the attitude code and temperature distribution of the main reflector, with  $128 \times 128 \times 2$  pixels; the output of the model is the deformation of the main reflector, with  $128 \times 128 \times 1$  pixels. (ii) There are many ways to improve the performance of CNN,

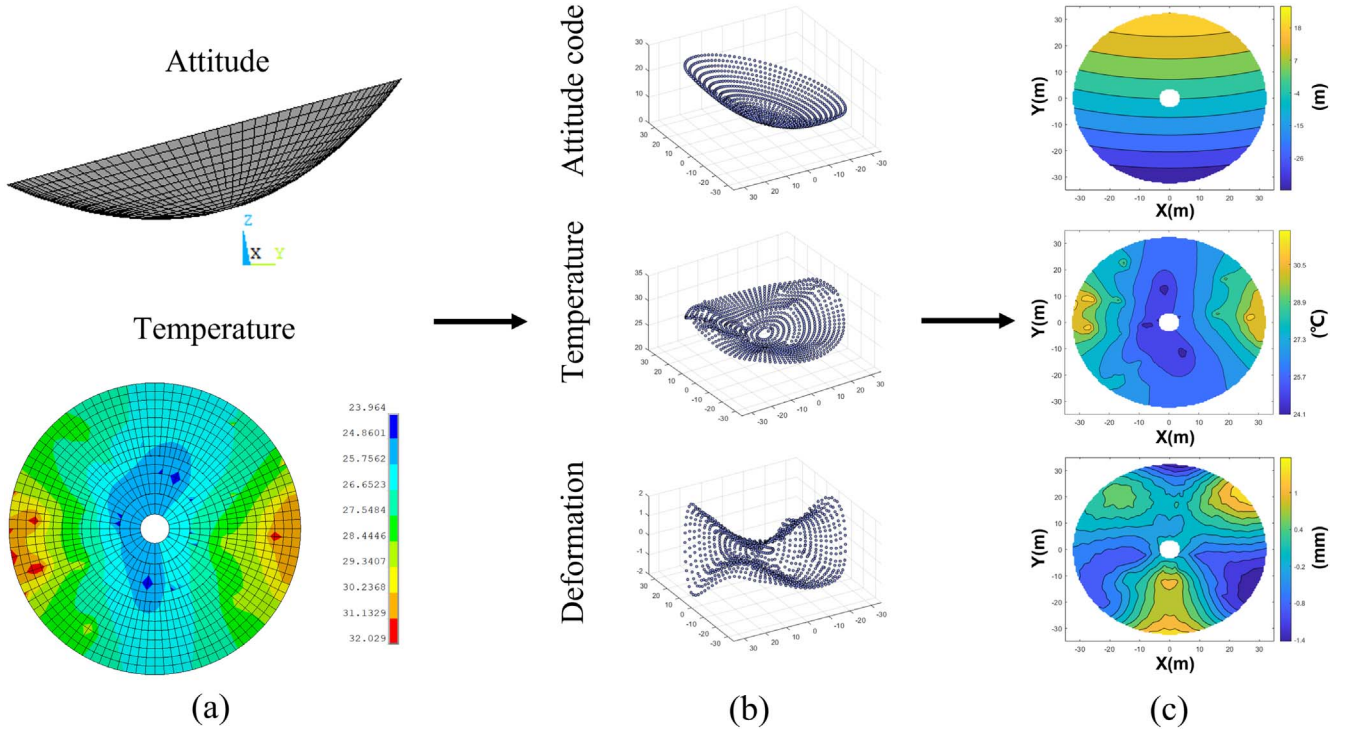


**Figure 9.** Data processing, including (a) the attitude and temperature of the main reflector, (b) the input and output data represented by a discrete set of nodes, and (c) prepared  $128 \times 128$  images for deep CNN training, validating, and testing.

especially increasing the depth and width of the CNN (Szegedy et al. 2015); besides this, kernel size, activation function, optimizer, learning rate, and strides also affect the performance of the CNN. (iii) As the complexity of the network increases, the problems (e.g., vanishing gradient, exploding gradient, and degradation) will also arise (Nielsen 2015).

In recent years, numerous studies have proven CNNs with U-shaped structures to be an effective architecture for image-to-image mapping (Mendoza et al. 2021; Romaszko et al. 2021; Tong et al. 2021; Zhou et al. 2022). A typical U-Net (Ronneberger et al. 2015) structure contains an encoder part and a decoder part for downsampling and upsampling, respectively. Moreover, skip connections, which can prevent feature information loss, link the encoder feature channels and the decoder feature channels with the same size. Through the improvement of U-Net, a U-Net with residual blocks (abbreviated as Res-U-Net) was developed for computing the deformation distribution, as shown in Figure 10. The Res-U-Net can be divided into encoder, residual learning module, and decoder. For all convolutional layers, we used  $3 \times 3$  kernel size, which can make the network have fewer training parameters than larger kernel size under the same receptive field (Simonyan & Zisserman 2014). Except for the final layer, each convolutional layer is followed by a batch-normalization layer and a scaled exponential linear unit (selu), which help the network to converge rapidly and suppress gradient anomalies,

respectively (Nwankpa et al. 2018). In each downsampling, the convolutional layer with stride 1 for feature extraction is first performed, and then a downsampling layer is used to compress the size of feature images. It is to be noted that the downsampling layer is composed of a convolutional layer with stride 2 instead of the traditional pooling layer. This is because the convolutional layer with stride 2 can retain feature information better (Tong et al. 2021). The decoder part is used to calculate the deformation distribution. The residual learning module, which is established in the region between the encoder and the decoder, contains six residual blocks and effectively solves the degradation problem caused by excessive network depth. Each residual block contains two convolutional layers and three batch-normalization layers. The residual block can be realized by feed-forward neural networks with “shortcut connections” (He et al. 2016).

### 5.3. Training of the Deep CNN Model

All 5000 samples were divided into training, validation, and test data sets in the same proportion (3:1:1) as before. The proposed deep CNN was trained in the Keras backend framework. In the training process, the mean squared error (MSE) was selected as the loss function, which is defined by:

$$\text{MSE} = \frac{\sum_{i=1}^N (\delta_i - \tilde{\delta}_i)^2}{N} \quad (16)$$

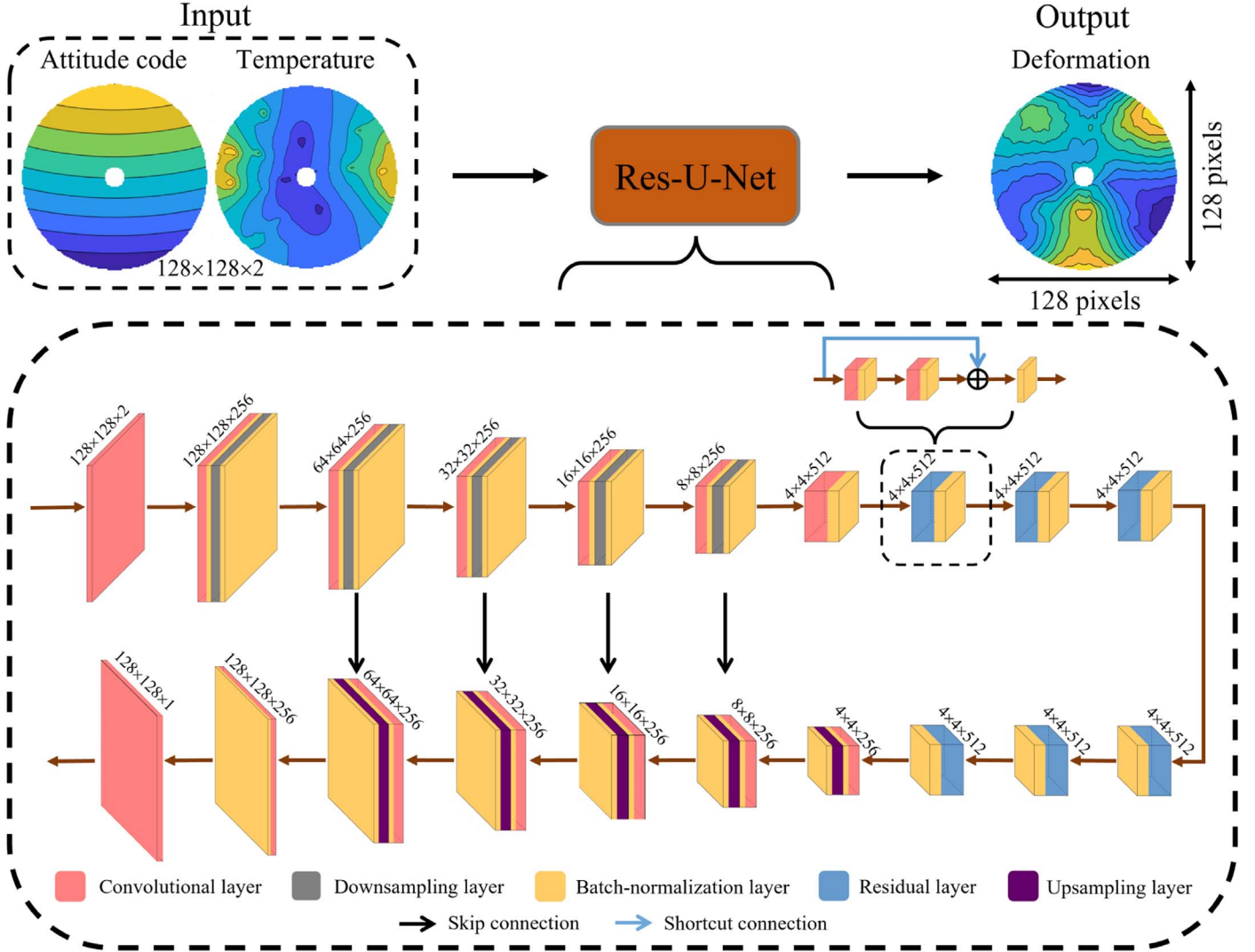


Figure 10. Res-U-Net architecture of the neural network.

where  $\delta_i$  is a deformation value at pixel node  $i$  calculated from FE simulation,  $\tilde{\delta}_i$  is a deformation value estimated from the deep CNN model,  $N$  is the number of all pixels.

Moreover, the Adam optimizer (Kingma & Ba 2014) with default parameters of  $\beta_1 = 0.9$  and  $\beta_2 = 0.999$  was selected for optimizing the loss function, and the initial learning rate was 0.001. The Keras callback APIs were employed to adjust the learning rate and terminate the training process early by monitoring the trend of the validation loss.

#### 5.4. Evaluation of the Deep CNN Model

In this paper, three performance metrics were used to evaluate the accuracy of the deformation distribution estimated by the deep CNN model: root mean square error (rms), relative root mean square error (RRMS), and image structural similarity

(SSIM). The image structural similarity, ranging from 0 to 1, can offset the defect that rms and RRMS cannot measure the similarity of deformation distribution structure. For each sample, rms, RRMS, and SSIM are defined as Equations (17), (18), and (19), respectively.

$$\text{RMS} = \sqrt{\text{MSE}} = \sqrt{\frac{\sum_{i=1}^N (\delta_i - \tilde{\delta}_i)^2}{N}} \quad (17)$$

$$\text{RRMS} = \frac{\text{RMS}}{\delta_{\max} - \delta_{\min}} \quad (18)$$

where  $\delta_{\max}$  is the maximum deformation,  $\delta_{\min}$  is the minimum deformation.

$$\text{SSIM} = \frac{(2\mu_r\mu_e + c_1)(2\sigma_{r,e} + c_2)}{(\mu_r^2 + \mu_e^2 + c_1)(\sigma_r^2 + \sigma_e^2 + c_2)}, \quad (19)$$

**Table 1**

The Performance of the Algorithms on the Test Dataset with Different Number of Features Points

Number of Points	rms/ $^{\circ}\text{C}$			RRMS		
	XGBoost	SVM	RF	XGBoost	SVM	RF
10	1.99	2.27	2.06	11.76%	13.50%	12.05%
30	0.80	1.97	1.75	4.75%	11.73%	10.17%
60	0.56	1.94	1.69	3.31%	11.68%	9.82%
80	0.47	1.92	1.67	2.82%	11.64%	9.66%
120	0.38	1.89	1.62	2.29%	11.53%	9.41%

where  $\mu_r$  and  $\mu_e$  are the mean values of deformation distribution images calculated from FE simulation and deep CNN model respectively,  $\sigma_r$  and  $\sigma_e$  are the standard deviations of deformation distribution images,  $\sigma_{r,e}$  is the covariance of deformation distribution images calculated from FE simulation and deep CNN model,  $c_1$  and  $c_2$  are small constants to avoid system errors caused by the denominator equal to zero.

## 6. Results

In this paper, all computations were performed on a PC with an Intel i7-8700 CPU and 16 GB of RAM, which is equipped with an NVIDIA GeForce GTX 1660Ti Graphics Cards.

### 6.1. Effectiveness of the Temperature Mapping Model

To highlight the advantages of XGBoost, two other methods, support vector machine (SVM) and random forest regressor (RF), were compared with the XGBoost algorithm. Table 1 presents the estimation accuracy of three models for the test data set with different numbers of feature points. The results showed that XGBoost has higher estimation accuracy than the other two methods. Considering the number of feature points and the estimation accuracy, 60 feature points were selected as the location of the temperature sensors. Using the grid search method, we obtained a set of hyperparameters with the best results, achieving low rms (avg, 0.56  $^{\circ}\text{C}$ ) and low RRMS (avg, 3.31%) simultaneously. The subsample and the maximum depth of trees were set as 0.6 and 10 respectively, and the other hyperparameters were set as the default values. The discrete temperature data in the test data set were converted to images by interpolation to visually compare the temperature distributions generated by FE simulation and XGBoost algorithm. Figure 11 shows four samples sampled from the test data set.

### 6.2. Effectiveness of the Deep CNN Model

The deformation distributions calculated by the FE simulation were considered approximate true data and compared with the deformation values predicted by the deep CNN model. The curve of training loss and validation loss over epochs can preliminarily verify the training effect of the deep

CNN model, as shown in Figure 12. Overall, the loss curve converges at the 120th epoch, and the training time is about 8h. Res-U-Net exhibited an excellent performance on the test data set, achieving low rms (avg, 96.28  $\mu\text{m}$ ), RRMS (avg, 2.37%), and high SSIM (avg, 0.9977) simultaneously, and the statistical charts are shown in Figure 13. Moreover, the approximate true deformation distribution, the Res-U-Net estimation, and the pixel differences between the two distributions are shown in Figure 14, while the performance metrics are reported in Table 2. From the difference distribution, it can be seen that the difference in deformation distributions of the main reflector calculated by the two methods is almost zero, and there is no extreme local difference.

### 6.3. Effectiveness of the Surrogate Model

To verify the accuracy and rapidity of the surrogate model, we executed the entire workflow in Figure 2 and the inputs of the surrogate model were the elevation angle and the temperature values of 60 feature points. The regenerated test data set including 100 samples was used to compare the time required for the FE analysis and the surrogate model method and display the similarity of the deformation distributions obtained by these two methods. The results of the computation time comparison are shown in Figure 15. The average computation time for FE analysis is 23.79 s, while the time required for the surrogate model to perform the computation is 0.33 s. This strongly shows that our method has the ability to predict the deformation distribution of the main reflector quickly. It should be emphasized that the FE analysis computation time only includes the solving time of the FE software. Manual FE modeling, meshing and post-processing will take a longer time, several minutes or more.

The average performance metrics of the estimated deformation distribution are 99.72  $\mu\text{m}$  (rms), 2.55% (RRMS), and 0.9975 (SSIM), which indicate there is almost no discrepancy between the deformation distribution calculated by the FE simulation and estimated by the surrogate model. The results are visualized for four representative samples, as shown in Figure 16, and their performance metrics are shown in Table 3. The sample shown in Figure 16(iv) represents one of the worst performances in test samples, there are some minor differences, but the overall deformation distribution is very similar. From the results, once the surrogate model has learned the relationship between the compound load and the deformation distribution, FE analysis is no longer needed, replaced by the surrogate model.

## 7. Discussion

The surrogate model method has high requirements on the data, so we first generated a data set that contains a large number of samples with diverse loads. For gravity, the data set contains all the elevation angles of the antenna under operating

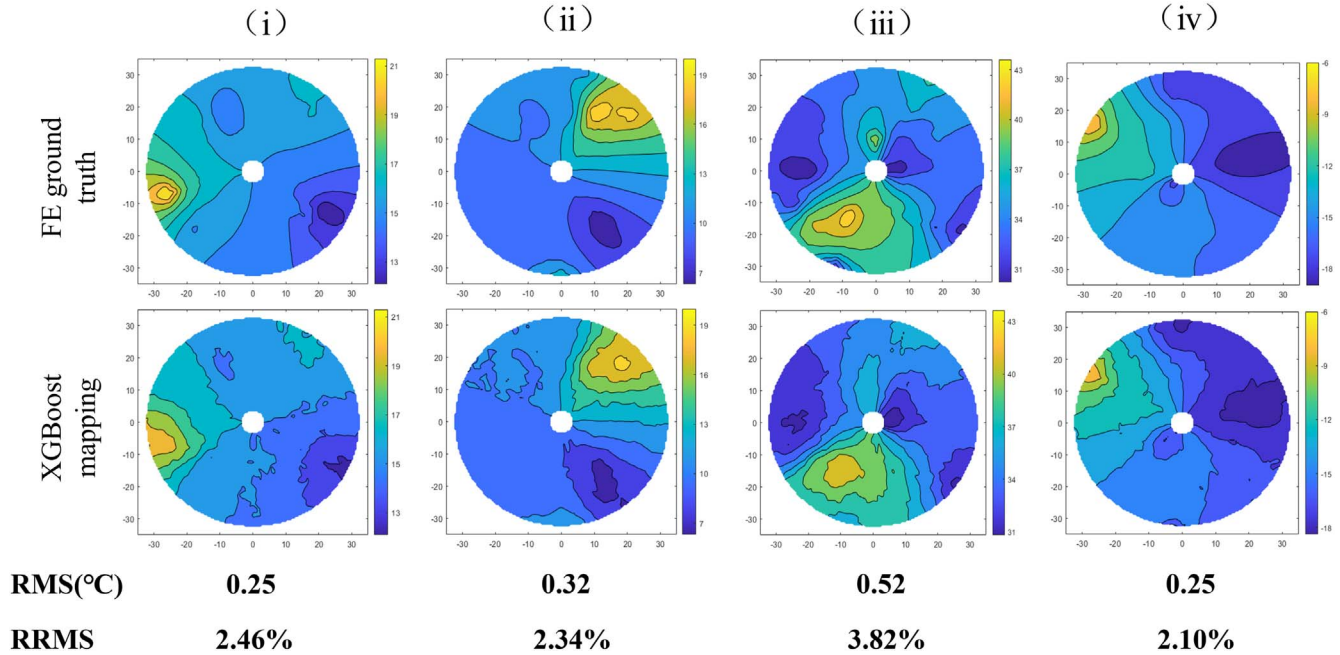


**Figure 11.** Comparison of temperature distributions obtained by the FE simulation and the method of this study.

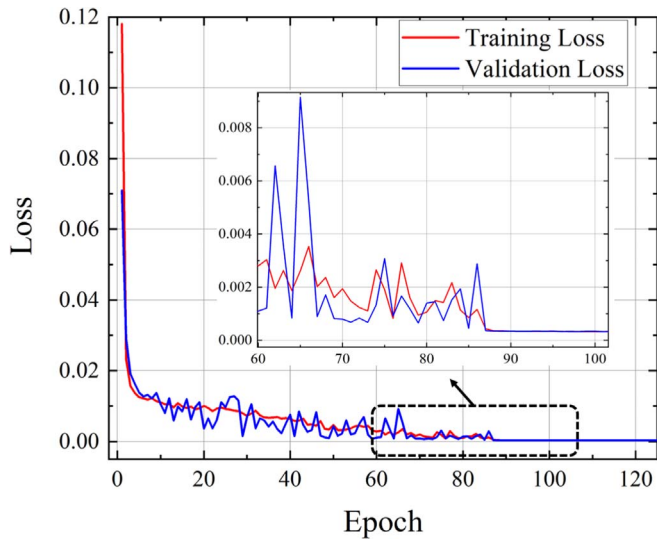


**Figure 12.** Deep CNN loss curve for the training process until convergence.

conditions to ensure the diversity of gravity distribution; for temperature, we obtain temperature samples by reasonably changing the antenna thermal environment. Although the temperature data are not actually measured, there are many temperature samples in our data set (such as the temperature distributions in Figure 5 and Figure 9) that are very similar to those obtained in recent antenna temperature studies (Liu 2016; Wei et al. 2021). Therefore, our data set can cover the key features of the considered loads. After training on the diverse

data set, the results strongly indicate that the surrogate model has learned the mapping between the gravity-thermal load and the deformation distribution of the main reflector. In this study, for the convenience of training, the surrogate model was divided into two modules. The two modules were trained and validated separately, and the regenerated test data set was used to test the accuracy of the entire surrogate model.

In the mapping module, the attitude code is obtained by a linear mapping that does not require training. For the temperature mapping, after selecting feature points and training the XGBoost model, the temperature distribution can be obtained accurately; the average rms and RRMS can reach 0.56 °C and 3.31% simultaneously. High-accuracy estimated temperature distribution is helpful for deformation calculation. The recent work of Wei et al. (2021) represents the latest research findings on the temperature distribution of the antenna. In this work, the heat exchange theory is used for the thermal analysis of the antenna, which has obtained satisfactory results. However, the thermal analysis based on the FE method cannot obtain the temperature distribution in real time. The feasibility of using the sparse sampling and XGBoost algorithm to solve the difficulty of obtaining the entire temperature distribution can provide a new method for the research of antenna thermal analysis. Hence, we are conducting further research to discuss using heat exchange theory as prior knowledge to obtain a more accurate temperature distribution. In the deformation calculation module, we develop a Res-U-Net with three parts: encoder, residual learning module, and decoder. Once the proposed network is trained, the deformation distribution

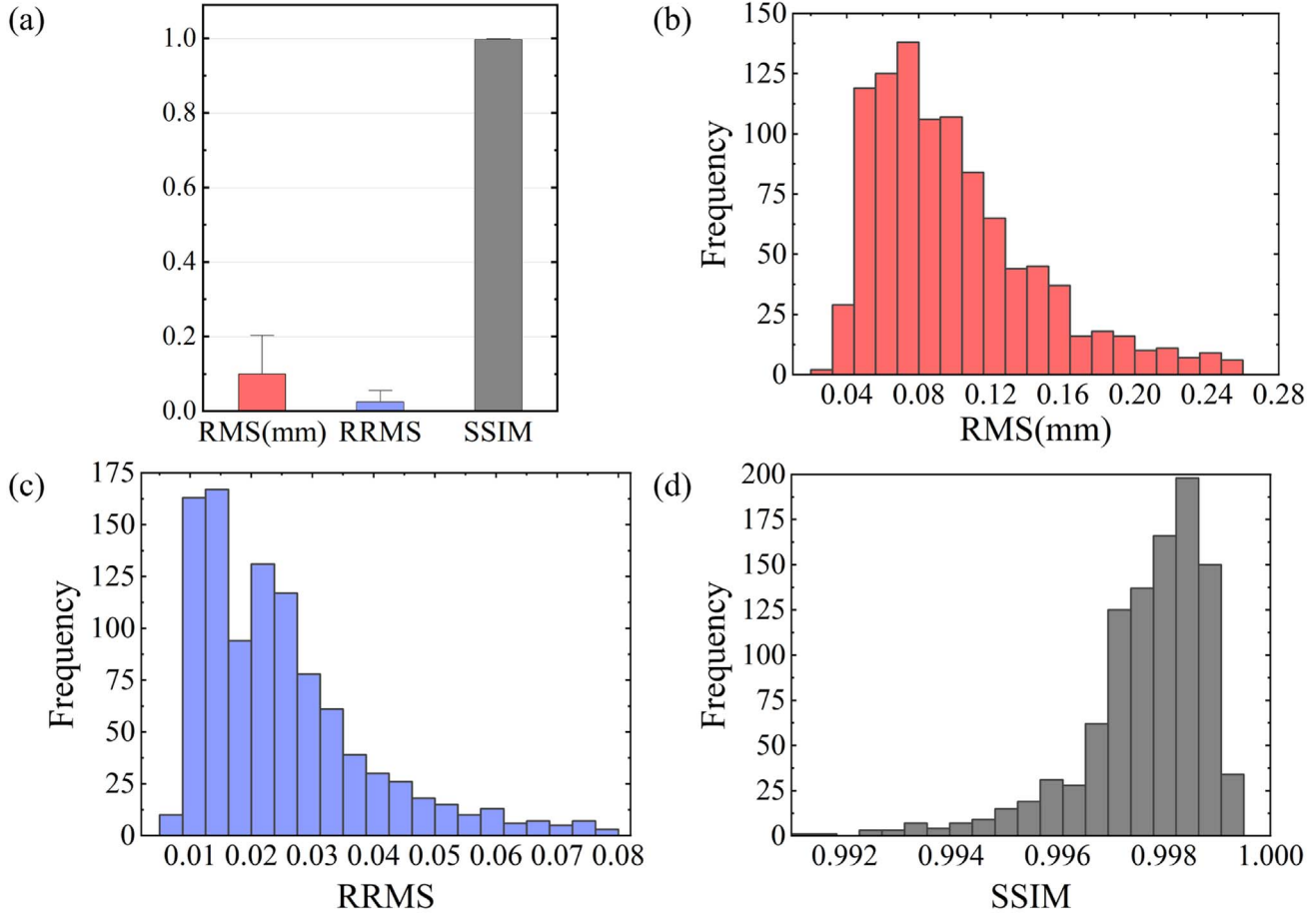


**Figure 13.** Statistical charts of the test data set, including (a) bar graph of the average rms, RRMS, and SSIM values, with error bars representing the standard deviation, (b) histogram of rms, (c) histogram of RRMS, and (d) histogram of SSIM.

calculated by Res-U-Net is highly consistent with the deformation distribution from the FE simulation. Moreover, there is no overfitting problem in the trained Res-U-Net, which is reflected in the performance of the network on the test data set, low rms (avg, 96.28  $\mu\text{m}$ ), RRMS (avg, 2.37%), and high SSIM (avg, 0.9977).

In the final test stage, when we regenerated samples and only used the elevation angle and sparse temperature data as the input of the surrogate model, after the calculation of the two modules, the deformation of the model output was still very similar to the deformation produced by the FE simulation. In practical application, our method is mainly divided into data acquisition system and deformation calculation system. First, the data acquisition system only needs to obtain the sparse temperature data from the temperature sensors and the current antenna attitude. There are 60 temperature sensors on the main reflector, the model is PT100, and the ZJ1064 multi-point temperature measuring instrument is used to collect temperature data. The ZJ1064 can be equipped with 64 temperature sensors at most at the same time, and the collection speed can

reach 30 temperature points per second. Therefore, a ZJ1064 can collect all temperature data in about 2 s. The current antenna attitude can be obtained at any time through the antenna monitoring system. Second, the deformation calculation system uses the collected data to calculate the deformation according to the process shown in Figure 2 which takes about 0.33 s. The surrogate model method does not require complex numerical simulation process like the FE method and iterative algorithm like the phase recovery method, so it greatly shortens the calculation time. Although the training of the model takes about 8h, it is a one-time process. In conclusion, our method is theoretically sufficient to resist the deformation that changes rapidly with time and meets the real-time requirement of large-aperture antenna deformation compensation.

To the best of our knowledge, this is the first study to use the surrogate model method based on machine learning and deep learning to rapidly and accurately estimate the temperature and deformation of an antenna’s main reflector. The motivation for this work is that the temperature analysis for large-aperture

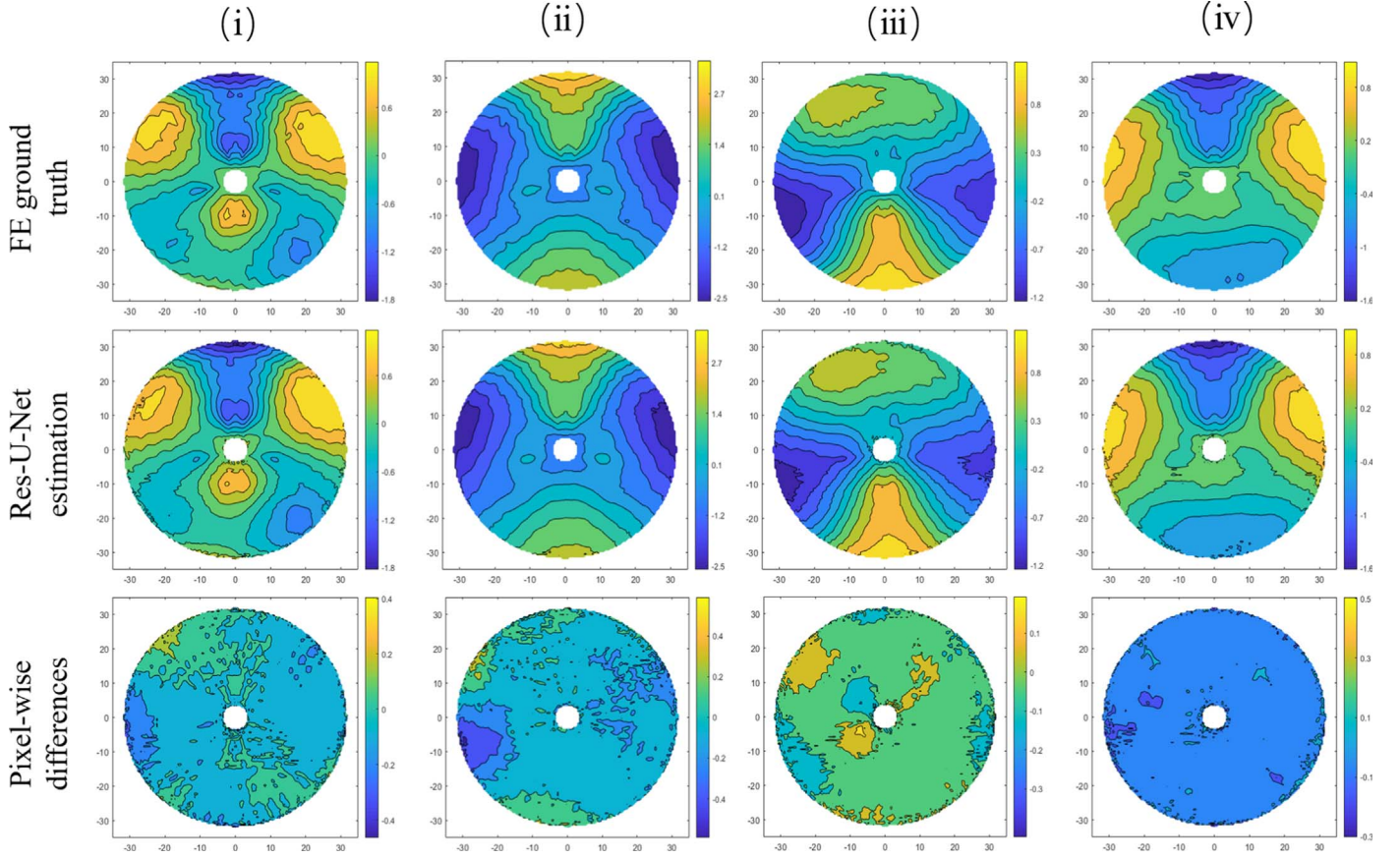


**Figure 14.** Deformation distributions from the FE simulation and the Res-U-Net, and the pixel-wise differences between them.

**Table 2**

Values of the Performance Metrics of the Samples Sampled from the Test Dataset

	rms/ $\mu\text{m}$	RRMS	SSIM
(i)	79.39	2.73%	0.9982
(ii)	114.26	2.19%	0.9972
(iii)	56.82	2.25%	0.9991
(iv)	54.92	2.08%	0.9991

antennas is still in the numerical analysis stage, and the manual FE deformation calculation of the antenna is time-consuming and complicated.

The limitations of this study are as follows: (i) this study is concerned about gravity-thermal-induced deformation but ignores wind loads. This is because the average wind loads mainly affect the pointing accuracy of the antenna rather than the surface accuracy (Xu et al. 2021). (ii) The purpose of this study is to evaluate the feasibility of the surrogate model to calculate the deformation distribution, so the FE model is simplified to facilitate the study. These limitations may lead to a slight deviation of the data set generated by the FE simulation from the actual deformation distribution of the main reflector.

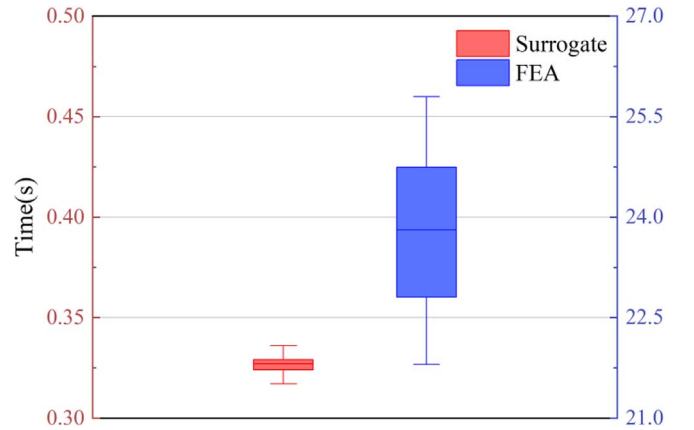


**Figure 15.** Computational time comparison between the FE simulation (excluding pre-processing and post-processing) and the surrogate model method: the five lines from top to bottom in the box plot represent the maximum, upper quartile, median, lower quartile, and minimum.

However, these limitations can be addressed in future work. Because the research on the effect of wind loads on the antenna structure becomes more mature, a comprehensive dynamic load including gravity, heat, and wind can be considered as the input

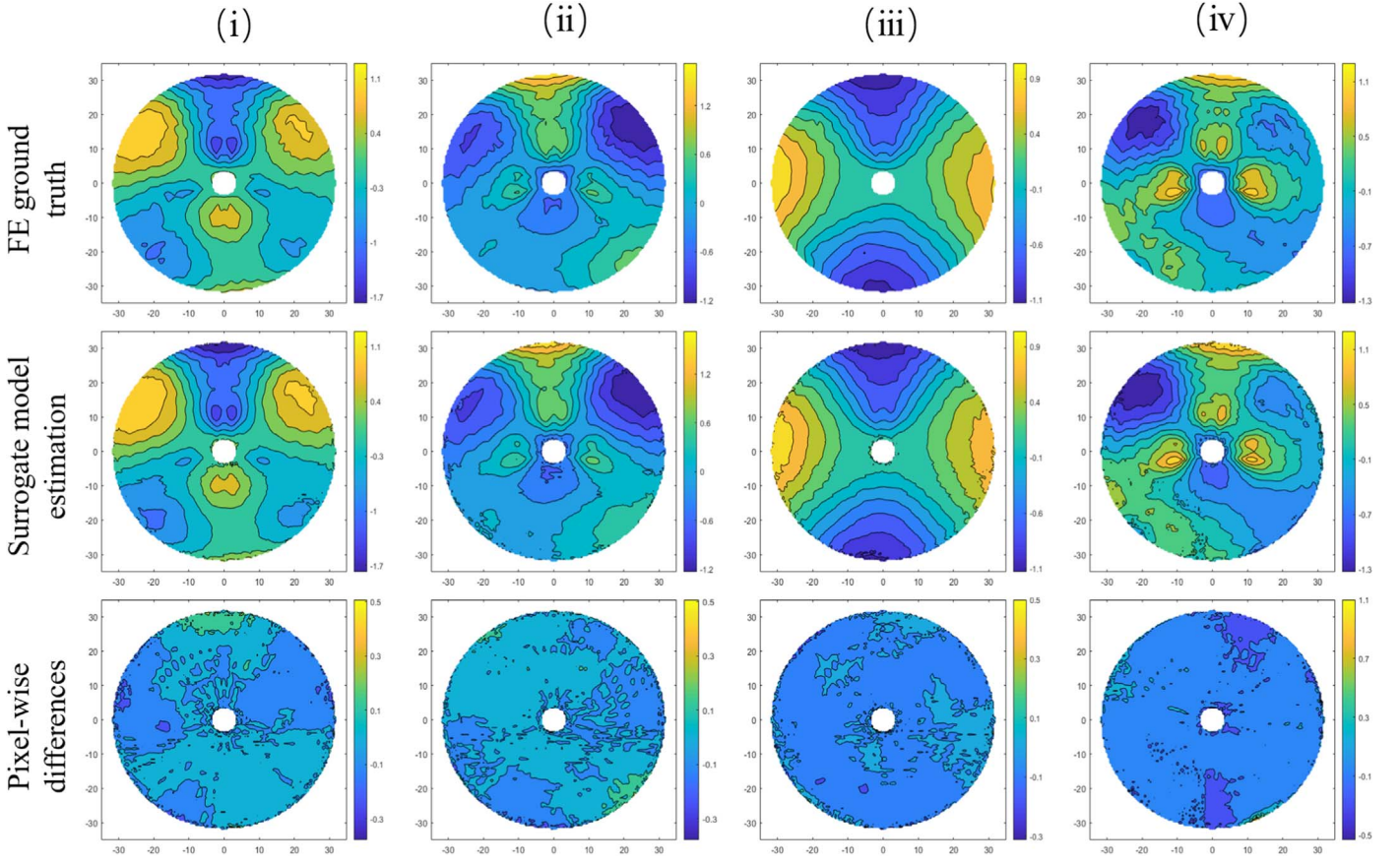


Figure 16. The visualized results of the regenerated test data set.

Table 3

Values of the Performance Metrics of the Samples Sampled from the Regenerated Test Dataset

	rms/ $\mu\text{m}$	RRMS	SSIM
(i)	85.68	2.33%	0.9983
(ii)	71.52	2.02%	0.9984
(iii)	57.11	2.11%	0.9992
(iv)	122.21	3.91%	0.9967

of the surrogate model in the follow-up research. In addition, based on the ability of neural networks to perform transfer learning, the performance of CNN can be further improved by using data sets obtained by more accurate deformation measurements. This is also one of the advantages of the surrogate model method.

## 8. Conclusion

This paper has proposed a novel surrogate model method to calculate the deformation distribution of the main reflector of the antenna. According to the conducted research, the main conclusions are as follows:

(i) A two-module surrogate model is proposed. The first module maps the sparse input information to the attitude code and temperature distribution of the entire main reflector, and the second module calculates the deformation distribution.

(ii) To solve the problem that the temperature distribution is difficult to obtain, a new temperature measurement method, which could predict the entire temperature distribution accurately with no more than 60 sampling points, is proposed.

(iii) A deep CNN with residual blocks is used to accurately complete the deformation distribution estimation in real time from temperature distribution and attitude code of the main reflector.

(iv) The final test results show that the surrogate model method can complete the calculation of the deformation distribution within 1 s, and the calculation results of the surrogate model are indistinguishable from the FE simulation results.

The method proposed in this study can obtain the surface accuracy of the main reflector of the antenna with a limited amount of data and does not require researchers to spend too much time learning the professional knowledge of the deformation calculation of the main reflector. In the follow-

up work, the estimation accuracy of the surrogate model can be further improved based on transfer learning.

### Acknowledgments

This work is supported by the National Key Basic Research and Development Program of China No. 2021YFC2203501, and the National Natural Science Foundation of China (project U1931137).

### ORCID iDs

Zi-Han Zhang  <https://orcid.org/0000-0001-6823-6667>

### References

- Attar, H. R., Zhou, H., Foster, A., & Li, N. 2021, *J. Manuf. Processes*, 68, 1650
- Bergstrand, S., Herbertsson, M., Rieck, C., et al. 2019, *JGeod*, 93, 669
- Chen, T., & Guestrin, C. 2016, in Proc. ACM SIGKDD Int. Conf. Knowledge Discovery and Data Mining (New York: Association for Computing Machinery), 785
- Dong, J., Fu, L., Liu, Q., & Shen, Z. 2018a, *ExA*, 45, 397
- Dong, J., & Liu, Q. 2021, *SSPMA*, 51, 029503
- Dong, J., Zhong, W., Wang, J., Liu, Q., & Shen, Z. 2018b, *ITAP*, 66, 2044
- Fan, J., Wang, X., Wu, L., et al. 2018, *Energy Convers. Manage.*, 164, 102
- Fu, L., Dong, J., Ling, Q., et al. 2017, *Chin. J. Radio. Sci.*, 32, 314
- Fu, L., Zhong, W., Qiao, H., Liu, G., & Qian, H. 2015, *AcASn*, 56, 378
- Greve, A., Bremer, M., Peñalver, J., Raffin, P., & Morris, D. 2005, *ITAP*, 53, 851
- Hartigan, J. A., & Wong, M. A. 1979, *J. Roy. Stat. Soc. C*, 28, 100
- He, K., Zhang, X., Ren, S., & Sun, J. 2016, in Proc. IEEE Computer Society Conf. Computer Vision and Pattern Recognition (Washington, DC: IEEE Computer Society), 770
- Hu, K. Y., Wang, K., Wu, P. Z., & Jiang, Y. 2017, *AMM*, 863, 266
- Kingma, D. P., & Ba, J. L. 2015, in Int. Conf. Learn. Represent., ICLR - Conf. Track Proc. (Ithaca, NY), 1
- Lee, S., Quagliato, L., Park, D., Berti, G. A., & Kim, N. 2021, *Metals*, 11, 1533
- Li, P., Duan, B., Wang, W., & Zheng, F. 2012, *IAPM*, 54, 40
- Lian, P., Duan, B., Wang, W., Xiang, B., & Hu, N. 2015, *ITAP*, 63, 2312
- Lian, P., Wang, C., Xue, S., et al. 2021, *ITAP*, 69, 6351
- Liang, L., Liu, M., Martin, C., Eleftheriades, J. A., & Sun, W. 2017, *Biomech. Model. Mechanobiol.*, 16, 1519
- Liang, L., Liu, M., Martin, C., & Sun, W. 2018, *J. Roy. Soc. Interf.*, 15, 20170844
- Liu, Y. 2016, *JApA*, 37, 1
- Mai, H. T., Kang, J., & Lee, J. 2021, *Finite Elem. Anal. Des.*, 196, 103572
- Mendoza, A., Trullo, R., & Wielhorski, Y. 2021, *Compos. Sci. Technol.*, 213, 108897
- Nielsen, M. A. 2015, *Neural Networks and Deep Learning*, Vol. 25 (San Francisco, CA: Determination Press)
- Nikolic, B., Hills, R., & Richer, J. 2007a, *A&A*, 465, 679
- Nikolic, B., Prestage, R., Baiser, D., Chandler, C., & Hills, R. 2007b, *A&A*, 465, 685
- Nwankpa, C., Ijomah, W., Gachagan, A., & Marshall, S. 2018, arXiv:1811.03378
- Qian, H., Liu, Y., Fan, F., Fu, L., & Liu, G. 2012, *Infr. Laser Eng.*, 41, 3027
- Qu, Y., Gong, Y., Ma, J., et al. 2020, *Environ. Pollut.*, 260, 114016
- Romaszko, L., Borowska, A., Lazarus, A., et al. 2021, *Artif. Intell. Med.*, 119, 102140
- Ronneberger, O., Fischer, P., & Brox, T. 2015, in Int. Conf. Medical Image Computing and Computer-Assisted Intervention, ed. A. F. Frangi et al. (Cham: Springer), 234
- Sato, H., & Igarashi, H. 2022, *COMPEL, Int. J. Comput. Math. Electr. Electron. Eng.*, 41, 900
- Sha, W., & Edwards, K. 2007, *Mater. Des.*, 28, 1747
- Simonyan, K., & Zisserman, A. 2014, arXiv:1409.1556
- Subrahmanyam, R. 2005, *ITAP*, 53, 2590
- Sun, Z.-X., Wang, J.-Q., Yu, L.-F., Gou, W., & Wang, G.-L. 2021, *RAA*, 21, 038
- Szegedy, C., Liu, W., Jia, Y., et al. 2015, in Proc. IEEE Computer Society Conf. Computer Vision and Pattern Recognition (Washington, DC: IEEE Computer Society), 1
- Tong, Z., Ye, Q., Xiao, D., & Meng, G. 2021, *OptLE*, 143, 106619
- Wang, B.-Y., Ye, Q., Fu, L., et al. 2022, *RAA*, 22, 035020
- Wang, C., Li, H., Ying, K., et al. 2018, *Int. J. Antennas Propag.*, 2018, 3412
- Wang, W., Wang, C., Duan, B., Leng, G., & Li, X. 2014, *IET Microwaves Antennas Propag.*, 8, 158
- Wei, S.-X., Kong, D.-Q., & Wang, Q.-M. 2021, *RAA*, 21, 293
- Wu, Z., Li, H., & Li, Q. 2021, *AIAAJ*, 59, 4669
- Xu, Q., Zhang, J., Wang, Z.-Y., & Pan, H.-Z. 2021, *RAA*, 21, 150
- Zheng, S., Wang, J., Zhuo, Y., Yang, D., & Liu, R. 2022, *Ecotoxicol. Environ. Safety*, 229, 113092
- Zhou, H., Xu, Q., Nie, Z., & Li, N. 2022, *J. Manuf. Sci. Eng.*, 144, 021012